TUMOR IMMUNOLOGY

Spatially mapping the immune landscape of melanoma using imaging mass cytometry

Dan Moldoveanu[1,2,3]†, LeeAnn Ramsay[1]†, Mathieu Lajoie[1]†, Luke Anderson-Trocme[4,5], Marine Lingrand[1,6], Diana Berry[1,6], Lucas J.M. Perus[1], Yuhong Wei[1], Cleber Moraes[1], Rached Alkallas[1,4,5], Shivshankari Rajkumar[1,6], Dongmei Zuo[1], Matthew Dankner[1], Eric Hongbo Xu[7], Nicholas R. Bertos[7], Hamed S. Najafabadi[4,5], Simon Gravel[4,5], Santiago Costantino[8], Martin J. Richer[9], Amanda W. Lund[10], Sonia V. Del Rincon[11,12], Alan Spatz[2,12,13], Wilson H. Miller Jr.[11,12], Rahima Jamal[14], Réjean Lapointe[14,15], Anne-Marie Mes-Masson[14,15], Simon Turcotte[14], Kevin Petrecca[16], Sinziana Dumitra[2,3,7], Ari-Nareg Meguerditchian[2,3,7], Keith Richardson[2], Francine Tremblay[2,3], Beatrice Wang[2,7], May Chergui[2], Marie-Christine Guiot[1,2,16], Kevin Watters[2], John Stagg[14], Daniela F. Quail[1,17], Catalin Mihalcioiu[2,7]‡, Sarkis Meterissian[2,3,7]‡, Ian R. Watson[1,6,7]*

Melanoma is an immunogenic cancer with a high response rate to immune checkpoint inhibitors (ICIs). It harbors a high mutation burden compared with other cancers and, as a result, has abundant tumor-infiltrating lymphocytes (TILs) within its microenvironment. However, understanding the complex interplay between the stroma, tumor cells, and distinct TIL subsets remains a substantial challenge in immune oncology. To properly study this interplay, quantifying spatial relationships of multiple cell types within the tumor microenvironment is crucial. To address this, we used cytometry time-of-flight (CyTOF) imaging mass cytometry (IMC) to simultaneously quantify the expression of 35 protein markers, characterizing the microenvironment of 5 benign nevi and 67 melanomas. We profiled more than 220,000 individual cells to identify melanoma, lymphocyte subsets, macrophage/monocyte, and stromal cell populations, allowing for in-depth spatial quantification of the melanoma microenvironment. We found that within pretreatment melanomas, the abundance of proliferating antigen-experienced cytotoxic T cells (CD8$^+$CD45RO$^+$Ki67$^+$) and the proximity of antigen-experienced cytotoxic T cells to melanoma cells were associated with positive response to ICIs. Our study highlights the potential of multiplexed single-cell technology to quantify spatial cell-cell interactions within the tumor microenvironment to understand immune therapy responses.

INTRODUCTION

The complex interactions between tumor, stroma, and the immune system are key to cancer development. Cutaneous melanoma is characterized by a high mutation burden, neoantigen load, and a heterogeneous immune infiltrate (1). Melanomas use a number of strategies to evade immunosurveillance, including antigen-presenting cell (APC) dysfunction, immune checkpoint expression, and a tolerogenic microenvironment (2). The discovery and therapeutic targeting of immune checkpoints has been a breakthrough in the treatment of this malignancy (3–5). While it is increasingly apparent that the composition of the melanoma microenvironment plays an essential role (6), our

current understanding of the mechanisms of response and resistance to immune checkpoint inhibitors (ICIs) remains incomplete.

RNA sequencing studies have significantly contributed to our understanding of the melanoma microenvironment by identifying a number of determinants of ICI response. For instance, bulk RNA sequencing of patient samples reveals an innate anti-PD1 resistance (IPRES) signature (7). At the single-cell level, RNA sequencing shows that melanoma tumor cells can express a T cell exclusion program, which correlates with poor response to anti-PD1 therapy. Furthermore, expression of the TCF7 transcription factor by CD8$^+$ cytotoxic T cells is predictive of a favorable clinical outcome in ICI-treated patients (8).

A number of studies have used single-cell protein expression approaches to identify correlates of ICI response in dissociated tissues. For example, flow cytometry time-of-flight (CyTOF) profiling of peripheral blood mononuclear cells (PBMCs) identifies pretreatment monocyte and natural killer subsets that correlate with ICI response (9, 10). CyTOF flow analysis of dissociated melanomas found distinct cellular mechanisms between different ICI therapies (11, 12). Specifically, anti-PD1 and CTLA4 ICIs both target subsets of exhausted-like CD8 T cells (CD45RO$^+$PD1$^+$TBET$^+$EOMES$^+$), whereas anti-CTLA4 therapies expand an ICOS$^+$ T helper 1 (T$_H$1)–like CD4 effector population (12).

An important limitation of single-cell sequencing and multiplexed flow cytometry approaches is their inability to capture spatial information. The organization of the tumor microenvironment is predictive and prognostic in multiple malignancies. For instance, the proximity of PD1 to its PD-L1 ligand correlates with improved response to anti-PD1 immunotherapy in multiplexed immunofluorescence analyses of pretreatment melanoma samples (6). Furthermore,

[1]Rosalind and Morris Goodman Cancer Institute, McGill University, Montréal, QC, Canada. [2]McGill University Health Centre, Montréal, QC, Canada. [3]Department of Surgery, Division of General Surgery, McGill University, Montréal, QC, Canada. [4]McGill University Genome Centre, Montréal, QC, Canada. [5]Department of Human Genetics, McGill University, Montréal, QC, Canada. [6]Department of Biochemistry, McGill University, Montréal, QC, Canada. [7]Research Institute of the McGill University Health Centre, Montréal, QC, Canada. [8]Hôpital Maisonneuve-Rosemont, Montréal, QC, Canada. [9]Indiana University School of Medicine, Indianapolis, IN, USA. [10]Ronald O. Perelman Department of Dermatology and Department of Pathology, NYU Grossman School of Medicine, New York, NY, USA. [11]Jewish General Hospital, McGill University, Montréal, QC, Canada. [12]Lady Davis Institute for Medical Research, Montréal, QC, Canada. [13]McGill University, Montréal, QC, Canada. [14]Centre de recherche du Centre Hospitalier de l'Université de Montréal (CRCHUM) and Institut du Cancer de Montréal, Montréal, QC, Canada. [15]Département de Médecine, Faculté de Médecine, Université de Montréal, Montréal, QC, Canada. [16]Montreal Neurological Institute and Hospital, Montréal, QC, Canada. [17]Department of Physiology, McGill University, Montréal, QC, Canada.

*Corresponding author. Email: ian.watson2@mcgill.ca
†These authors contributed equally to this work.
‡These authors contributed equally to this work.

the location of CD8$^+$ lymphocytes in relation to the tumor border is linked to patient outcome in triple-negative breast cancer and cutaneous melanoma (6, 13, 14). While limited by the number of markers concurrently captured by fluorescence microscopy, these studies highlight the importance of preserving spatial information with multiplexed proteomic profiling of the tumor microenvironment (15, 16).

In this study, we used CyTOF imaging mass cytometry (IMC) to spatially quantify 35 proteins at subcellular resolution in 5 benign nevi and 67 melanomas, including 30 samples procured from patients before the start of ICI therapy. This approach allowed for a comprehensive characterization of immune cell organization within the tumor microenvironment. We observed a high degree of heterogeneity in the magnitude and the composition of the immune infiltrate, and described an overarching hierarchy in its organization. The abundance of tumor-infiltrating lymphocyte (TIL) subsets is associated with better prognosis and response to ICIs (17–19). Here, we found that of this TIL population, it was the enrichment of proliferating antigen-experienced cytotoxic T cells (CD8$^+$CD45RO$^+$Ki67$^+$) within the pretreatment melanoma microenvironment that was associated with ICI response. Furthermore, the proximity and contact frequency between antigen-experienced cytotoxic T cells and melanoma cells was a significant spatial determinant of ICI response in pretreatment samples.

RESULTS
Development of a multiplexed antibody panel to characterize the melanoma microenvironment
Our CyTOF IMC profiling used tissue microarray (TMA) slides containing multiple samples stained with a cocktail of 35 antibodies labeled with unique metal isotopes (Fig. 1A and tables S1 to S3). A high-energy laser ablated slides 1 μm^2 at a time, converting the tissue into ionized plumes. These plumes were then processed in a TOF mass spectrometer, deriving isotope counts for each ablated spot. This information was then used to reconstruct a stack of 35 images, reflecting each antibody staining pattern. To develop an antibody panel that could extensively characterize the melanoma microenvironment, we selected antibodies commonly used for immunohistochemistry and immunofluorescence applications, including clinically used clones (e.g., SP142 for PD-L1 and 4C4.9 for S100), for the CyTOF IMC platform. We prioritized antibodies recognizing phenotypic markers to delineate the immune infiltrate (CD3, CD4, CD8, CD20, and CD68), along with selected immune checkpoints (CD40, ICOS, LAG3, TIM3, PD-L1, and VISTA), melanoma markers (SOX10 and S100), and stromal markers (CD31 for endothelial cells) (Fig. 1A). We also included antibodies against key melanoma signaling pathway regulators {β-catenin and total and phosphorylated ERK (extracellular signal–regulated kinase) and MEK [mitogen-activated protein kinase (MAPK) kinase]} and phenotypic events (Ki67 to measure proliferative status). The antibodies used in our panel were initially validated in spleen and melanoma tissue to confirm affinity and specificity of binding (Fig. 1, B to G, and see the "Antibody validation" section in Materials and Methods). As expected, we observed CD68 and CD3 expression to be mutually exclusive and localized to the cytoplasm and cell membrane in a spleen sample (Fig. 1E). Similarly, CD4 and CD8 (markers of T helper and cytotoxic T cells, respectively) were mutually exclusive, whereas FoxP3 yielded a nuclear signal and was coexpressed with CD4, as expected for regulatory T cells (T$_{regs}$) (Fig. 1F). S100 and SOX10 both stained melanoma cells, and were thus frequently coexpressed, while remaining mutually exclusive to the lymphocytic marker CD3 (Fig. 1G).

The histological architecture of normal and malignant tissue was also used to validate antibody binding. As expected, germinal centers in the spleen had a high number of CD20-positive B cells, whereas the surrounding corona was predominantly populated with CD4-positive T helper cells and CD68-positive macrophages (Fig. 1D). Vessel-like structures stained positive for CD31 across multiple tissue samples (example in Fig. 1B). SOX10 expression in melanoma cells was confined to the nucleus, whereas S100 staining was predominantly cytoplasmic and mirrored the appearance of melanoma cells seen in immunohistochemistry preparations (Fig. 1, C and G). In summary, the antibodies used in this study provided markers to identify melanoma, lymphocyte subsets, macrophage/monocyte, and stromal cell populations as well as expression of key signaling pathways and immune checkpoints.

Establishment of an analysis pipeline to characterize the spatial immune landscape of melanoma
To gain a comprehensive view of the melanoma microenvironment at various stages of disease and across different melanoma subtypes, we first applied our CyTOF IMC profiling platform to characterize a commercially available cohort of 42 melanocytic neoplasms, which included 5 benign nevi, 6 primary acral, 7 non-acral cutaneous, and 13 mucosal melanomas, as well as 11 lymph node metastases (note that this cohort did not receive ICI therapy). However, to identify correlates of ICI response, we profiled pretreatment melanoma samples from 30 patients with advanced disease who subsequently received ICI therapy (8 treated with anti-PD1, 17 with anti-CTLA4, and 5 with both anti-PD1 and CTLA4 in this ICI-treated cohort). Treatment response was determined by the immune-related response criteria (irRC) (table S1) (20). Fourteen patients demonstrated a response to ICI therapy, which was defined as either a complete response (CR), partial response (PR), or stable disease (SD). Sixteen patients had progressive disease (PD) and were considered nonresponders.

To convert the raw IMC images into single-cell data, we optimized a data analysis pipeline (21) for our dataset (Fig. 2A and fig. S1A). We used nuclear channels (histone H3 and iridium) to identify cell nuclei, which served as the basis for cell segmentation, and computed average marker intensities for each individual cell. Next, we applied PhenoGraph (22) and k-means clustering on the intensities of 10 lineage markers (CD45, CD3, CD4, CD8, CD20, CD68, CD14, SOX10, S100, and CD31) to initially classify cells into six lineages: CD8$^+$ cytotoxic T cells (Tc), CD4$^+$ T helper cells (Th), macrophage and monocytes (macro.mono; CD68$^+$ or CD14$^+$), B cells (B; CD20$^+$), melanoma and melanocytes (melano; SOX10$^+$ or S100$^+$), and endothelial cells (CD31$^+$). Cells that did not express any of the aforementioned markers or with conflicting expression patterns were classified as "others" (see the "Cell reassignment of ICI-treated dataset" section in Materials and Methods). This initial classification was further refined using positivity for FoxP3 and CD45RO, as determined by the ilastik supervised learning algorithm (23), to identify T$_{regs}$ (CD4$^+$FoxP3$^+$) (24) and discriminate between naive (Tc.naive and Th.naive; CD45RO$^-$) and antigen-experienced (Tc.ae and Th.ae; CD45RO$^+$) cytotoxic and helper T cells (fig. S1A; resulting mean marker intensities in Fig. 2B for ICI-treated cohort and fig. S1B for non–ICI-treated cohort) (25). To assess the quality of our cell classification, we compared the raw images with the
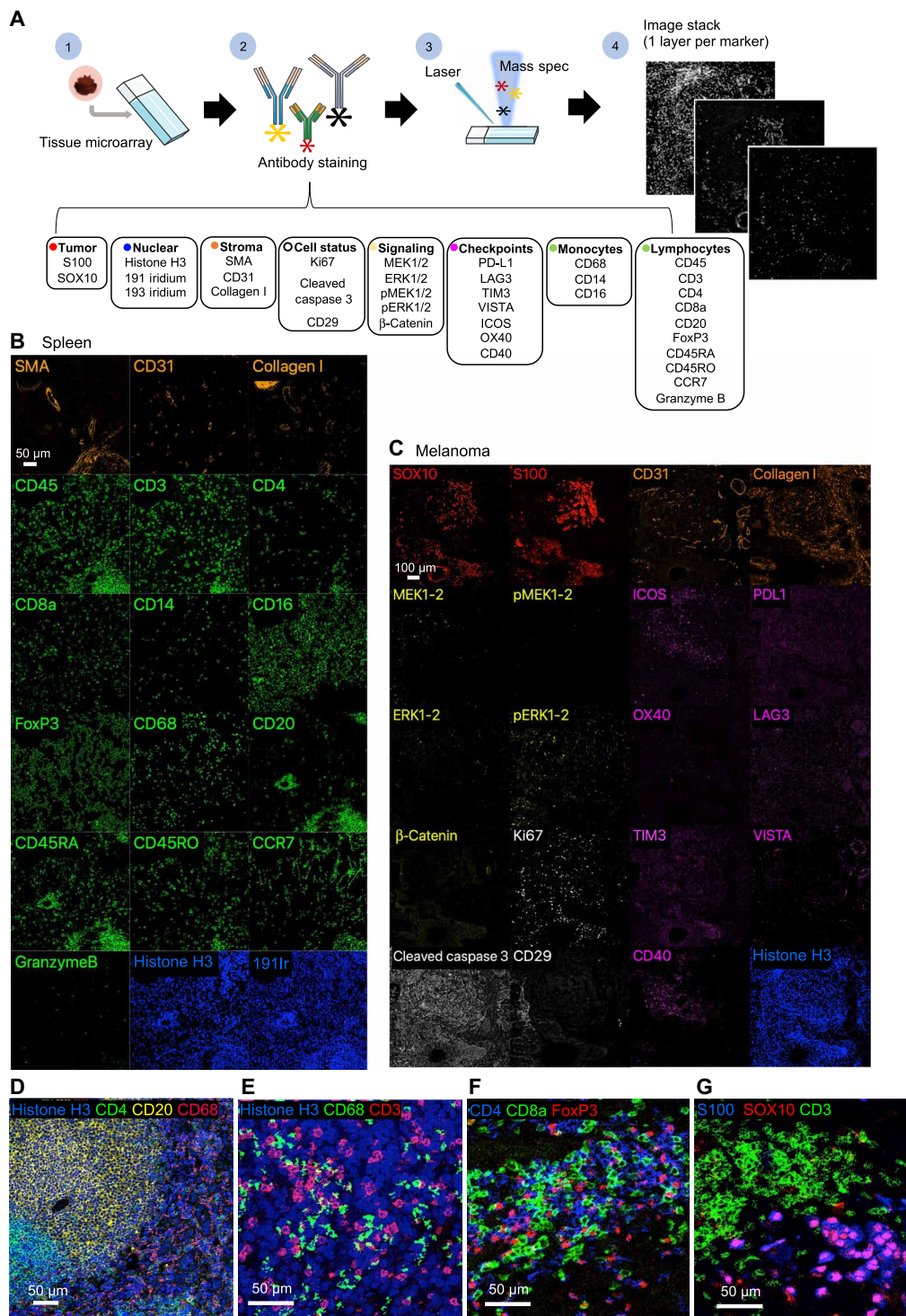
Fig. 1. Multiplexed CyTOF IMC marker panel to characterize the melanoma microenvironment. (A) Illustration of the data acquisition workflow used for CyTOF IMC: (1) One 4-μm-thick section of a TMA composed of 1-mm² melanoma cores (2) was stained with a cocktail of 35 antibodies labeled with metal isotopes (colored asterisks). (3) Samples were then ablated with a high-energy laser in a rastered pattern. The resulting ionized isotope plumes were analyzed by a mass cytometer, which returned the number and type of metal isotopes per pixel. (4) Each antibody resulted in a single image per sample, and together constructed a multi-image stack. **(B)** Representative images of stroma (orange), immune (green), and nuclear (blue) markers from a spleen sample. Scale bar in upper left image. **(C)** Representative images of melanoma markers (red), immune checkpoints (purple), cell status markers (white), cell signaling (yellow), stroma (orange), and nuclear (blue) markers in a melanoma sample. Scale bar in upper left image. **(D)** Representative multicolor image of a spleen sample, illustrating the architecture of a germinal follicle along with its cell populations. **(E)** Color overlay of an image obtained in spleen showing signal for histone H3, CD68 (macrophage), and CD3 (lymphocyte) markers. **(F)** Image obtained from a melanoma sample showing signal for CD4 (T helper cells), CD8a (cytotoxic T cells), and FoxP3 (Tregs). **(G)** Image obtained from a melanoma samples showing signal for S100 and SOX10 (melanoma) with CD3 (lymphocyte).
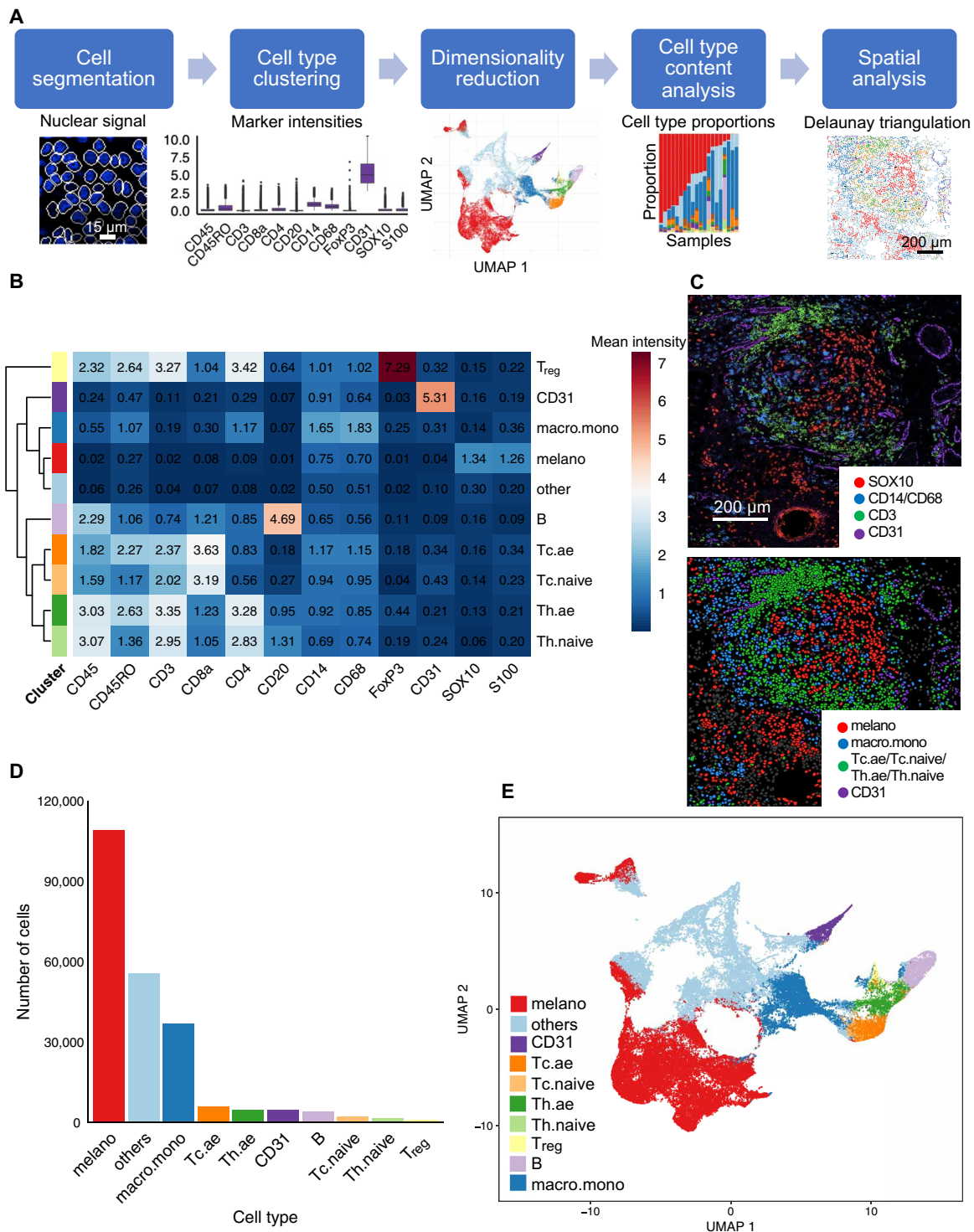
Fig. 2. Analysis pipeline to characterize the spatial immune landscape of melanoma. (**A**) Overview of the data analysis pipeline used in this study. Cells were first segmented to identify cellular location. They were then classified into 10 cell types based on the expression pattern of 12 lineage markers using *k*-means/PhenoGraph clustering and ilastik. Dimensionality reduction was performed using UMAP to visualize and assess the quality of the cell classification. Proportions of cell types were compared across clinical features and treatment groups. Spatial analyses were performed using the locations of cells within each tissue slide. (**B**) Heatmap of the mean intensity of each identity marker for each cell type in the ICI-treated cohort. Mean intensity is calculated per cell type from the normalized mean expression per cell. See fig. S1B for the non–ICI treated cohort. (**C**) Examples of raw (top) and processed (bottom) images for sample 26BL. Top: Raw signal intensities for melanoma (SOX10), macrophage/monocyte (CD14/CD68), lymphocyte (CD3), and endothelial (CD31) antibody markers. Bottom: Segmented cells labeled by cell types. (**D**) Total number of cells identified for each cell type in the combined cohort. (**E**) UMAP projection of all cells from the ICI-treated cohort using expression of the 12 identity markers. Cells are labeled according to the cell types identified through clustering. See fig. S1C for non–ICI treated cohort.

segmented/lineage-assigned image and observed clear agreement between staining patterns (Fig. 2C). In addition, we used the Uniform Manifold Approximation and Projection (UMAP) algorithm (26) to project all identified cells (Fig. 2E) on a two-dimensional plane reflecting the expression of our 12 identity markers, and found distinct clustering patterns recapitulating the identified cell types (Fig. 2E and figs. S1, C to E, S2, and S3). Our approach allowed for the localization and classification of more than 220,000 individual cells from 72 samples (fig. S4 and table S4), profiling the melanoma microenvironment at great depth.

Image analysis identified distinct immune infiltration patterns within melanoma samples

Having classified each cell into its respective subtype, we compared the immune landscape across samples. We found that immune infiltration patterns varied broadly, ranging from "immune-cold" tumors with few or no immune cells to strongly infiltrated tumors (Fig. 3, A and B). We observed trends toward fewer immune cells in nevi and acral melanomas, and more macrophages and monocytes in mucosal melanomas and lymph node metastases (fig. S5, A and B). Nevi and acral melanomas had a higher proportion of "other" cells that lacked signal from lineage markers used in our panel, likely due to the higher frequency of fibroblasts and keratinocytes, as evidenced by the global histological architecture of these areas (fig. S5C). However, within the immune component, nevi had a significantly higher fraction of naive cytotoxic T cells and T helper cells compared with primary and metastatic melanoma (fig. S5D). Although brain metastases made up only a small part of our cohort, these samples had a smaller immune component that was enriched in monocytes/macrophages (fig. S5, B and D).

Next, we examined immune cell composition differences between sexes, age groups, and across sites of distant metastasis. Previous studies report better anti-PD1 response in patients over 60 years old due to the presence of a proportionally higher number of T_{regs} and better responses in younger patients with higher T_{reg}–to–cytotoxic T cell ratios (27). In our dataset, we did not observe these relationships, likely due to the differences in sample size (fig. S6A). However, patients younger than 60 tended to have a higher proportion of melanoma cells within their microenvironment, suggesting purer, less immune infiltrated tumors. A recent report indicates that female patients with melanoma derive less clinical benefit from ICI therapy than do their male counterparts (28). We observed a number of trends in cell type proportion differences between sexes, but none reached statistical significance in our cohort (fig. S6B).

To better understand the global composition and organization of the melanoma immune landscape, we examined the presence and absence of immune cells within each sample (Fig. 3C; see Materials and Methods). The most common infiltrating cell lineage was macrophages/monocytes, followed by cytotoxic T cells and T helper cells. Cytotoxic T cells co-occurred with cells from the macrophage/monocyte lineage, and most patients with T helper cells concurrently had cytotoxic T cells and macrophages/monocytes within their tumor. T_{regs} and B cells were present in far fewer patients than the aforementioned cell types and were detected in only ~10% of samples. Similarly, these B cells and T_{regs} were almost always accompanied by the more common cell lineages described above (Fig. 3C). This hierarchical ordering was statistically significant on a Fisher's exact test and was robust to changing the thresholds used to determine cell type presence (fig. S6C).

Immune infiltrates rich in proliferating antigen-experienced cytotoxic T cells correlated favorably with immunotherapy response

To identify correlates of immunotherapy resistance, we first searched for common melanoma microenvironment features that correlated with response to anti-CTLA4 or anti-PD1 therapy, focusing on cell type–specific expression of the immune checkpoints VISTA, CD40, LAG3, OX40, ICOS, PD-L1, and TIM3. We started by performing clustering analysis on the expression of these markers in melanoma cells. As expected, melanoma cells expressed very little CD40, LAG3, OX40, and ICOS, and these markers contributed minimally to the clustering (Fig. 3D). Conversely, TIM3, PD-L1, and VISTA were the primary markers driving the separation of samples with up-regulated immune checkpoints (Fig. 3D, bottom cluster), from those with down-regulated checkpoints (Fig. 3D, top cluster). ICI nonresponders tended to express globally higher levels of immune checkpoints. However, no individual marker was significantly differentially expressed when comparing responders with nonresponders. Almost all cell types showed some level of expression of TIM3, with CD31, Tc.ae, and T_{regs} having more than 50% of their cells positive for TIM3 (fig. S7A). B cells were the only cell type with more than 50% of cells positive for CD40, and T_{regs} were the only cell type with more than 50% positivity for ICOS.

Several studies report that the degree of lymphocyte infiltration is correlated with patient outcome and response to immunotherapy in melanoma (17–19). As expected, we observed that samples with a high proportion of cytotoxic T cells and T helper cells showed a trend toward favorable treatment response. This trend was most pronounced in the subset of CD45RO$^+$ antigen-experienced T cells (Fig. 4A). These relationships also held if we restricted the analysis to samples with at least 250 melanoma cells (fig. S7, B to D). We compared expression of immune checkpoints as well as β-catenin and MAPK signaling markers (total and phosphorylated MEK and ERK), cleaved caspase 3, and Ki67 between responders and nonresponders across all cell types. Of these markers, only the presence of Ki67 on antigen-experienced cytotoxic T cells (Tc.ae) showed a significant association with improved ICI response ($P = 0.022$) (Fig. 4B). This relationship was also reflected in our survival analysis, as patients with a high proportion of Ki67$^+$ antigen-experienced T cells (i.e., above the median proportion) had improved survival ($P = 0.0019$) (Fig. 4C; representative image of Ki67$^+$ Tc.ae infiltration in Fig. 4D). This relationship held when we considered absolute cell counts instead of sample proportions (fig. S7E).

To validate our findings, we first performed immunofluorescence microscopy analysis on whole slides originating from the same samples as our ICI cohort characterized by CyTOF IMC. We stained for CD4, CD8, CD20, and FoxP3 markers on the whole tumor slide, which represented on average four times the area used in our CyTOF analysis. First, we found a significant correlation in cell type proportions when comparing subsampled regions from whole tumor slides, suggesting that smaller cores were generally representative of larger tumor areas (fig. S8A). Second, our analysis of additional regions from whole slide immunofluorescence data found significant correlations with the cell type proportions measured by CyTOF IMC (fig. S8B). Next, we performed immunofluorescence microscopy analysis on a validation cohort of 25 melanoma patients with cutaneous melanoma treated with ICIs (8 with anti-PD1, 13 with anti-CTLA4, and 4 with both anti-PD1 and anti-CTLA4). We found that the trend toward longer survival in patients with higher proportions of Ki67$^+$ Tc.ae held in this validation cohort (fig. S8C).
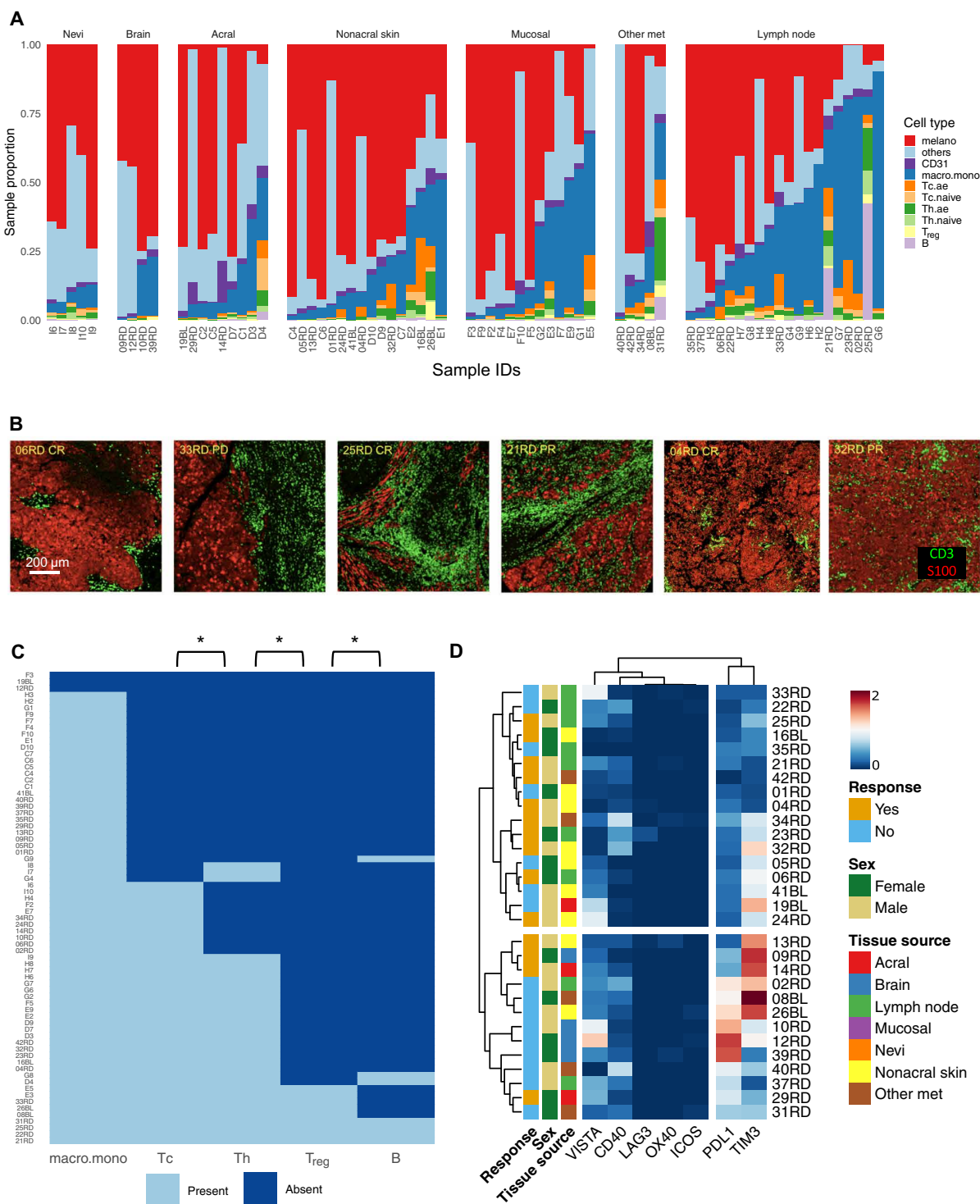
Fig. 3. Composition and organization of the melanoma immune microenvironment. (**A**) Stacked bar plots showing the proportion of each cell type in each sample. Samples are ordered by their total proportion of immune cells and grouped by subtype and tissue of origin. (**B**) Sample images demonstrating variation in T cell infiltration within tumors, ranging from well-compartmentalized (left) to diffusely infiltrated (right). (**C**) Co-occurrence matrix shows the presence of cell types in each sample in light blue, defined as at least 30 cells per lineage. Asterisks indicate significant co-occurrence relationships (corrected $P < 0.05$, Fisher's exact tests). For additional cutoff values and sample information, refer to fig. S6C. (**D**) Clustering of ICI-treated patients according to immune checkpoint expression in melanoma cells. Tissue source and patient sex are indicated, as well as treatment response.
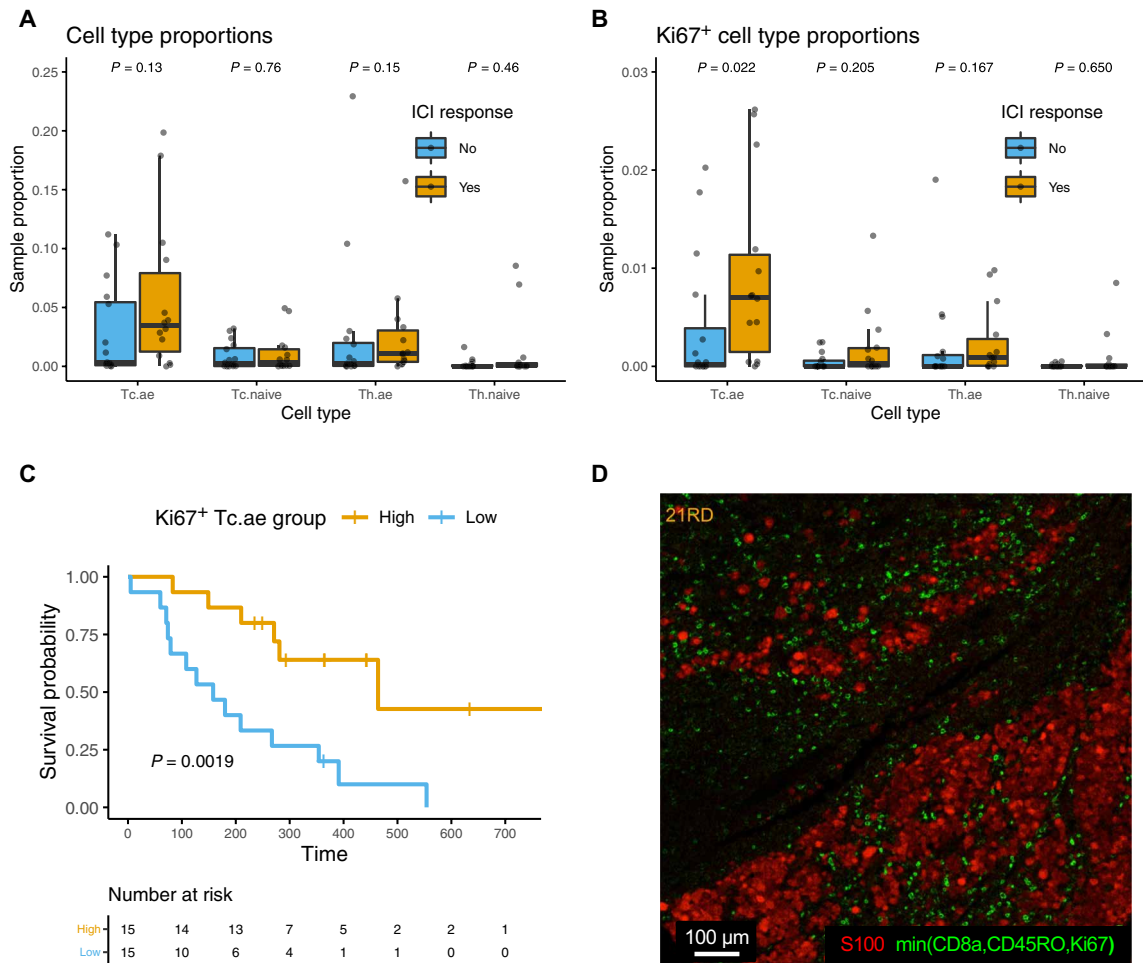
Fig. 4. Immune infiltrates rich in proliferating antigen-experienced cytotoxic T cells correlate favorably with immunotherapy response. (**A**) Cell type proportion for T cell subpopulations within the ICI-treated cohort ($N = 30$). Uncorrected P values from two-sided Wilcoxon rank sum test. (**B**) Proportion of Ki67^{+} T cell subpopulations within the ICI-treated cohort. Uncorrected P values from two-sided Wilcoxon rank sum test. (**C**) Kaplan-Meier survival curves comparing patients with a high proportion of Ki67^{+} Tc.ae cells (yellow) with those with a low proportion of Ki67^{+} Tc.ae cells (blue) within the ICI-treated cohort ($N = 30$). Uncorrected P value from Mantel-Haenszel log-rank test. (**D**) Sample image illustrating proliferating CD8^{+}CD45RO^{+}Ki67^{+} cells (green). To produce this image, we took the minimum intensity between the CD8, CD45RO, and Ki67 channels for each pixel. This highlights the cells that are simultaneously positive for these three markers. Melanoma cells are shown in red for the same sample using the S100 channel. Each channel was initially scaled using the 99th percentile of pixel intensities and smoothed using a Gaussian kernel.

Antigen-experienced T cells were closer in proximity to melanoma cells in pretreatment samples from immunotherapy responding patients

Next, we leveraged spatial information to quantify cell-cell interactions between the 10 identified cell types. For each tissue sample, we used Delaunay triangulation and a distance threshold of 30 μm to construct a spatial graph where nodes corresponded to cells and edges represented inferred contacts (Fig. 5A). Most cells had five or six immediate neighbors located at a median average distance of 16 μm (fig. S9, A and B). The physical distances between adjacent cells varied depending on the cell types, reflecting differences in their size and packing characteristics. The smallest distances were observed between pairs of lymphocytes (median of 13 μm), whereas the largest distances were observed between endothelial and melanoma cells (median of 18 μm) (Fig. 5B).

To further study the general spatial structure of the melanoma microenvironment, we partitioned the spatial graphs into regions

comprising connected cells from the same type (representative image in Fig. 5A). For all cell types, we observed that the size of these regions followed a heavy-tailed distribution, with more than 50% consisting of a single cell (Fig. 5C). However, the size distributions differed considerably across cell types. For instance, 50% of cells were found within large regions for melanoma (region size > 2031 cells), B cells (region size > 521 cells), and others (region size > 155 cells), whereas T lymphocytes and endothelial cells belonged mostly to small regions of one or two cells (Fig. 5D). Next, we quantified the tendency for cells of the same type to cluster together spatially within the tumors using the assortativity coefficient, an established measure used in graph theory (Fig. 5E) (29). A value of 1 would indicate perfect assortative mixing (i.e., contacts occur only between cells from the same type), a value of zero would indicate random mixing between cell types, and a negative value would indicate disassortative mixing (preference for contacts between cells from different types). While this metric controls for cell type proportions, we observed a
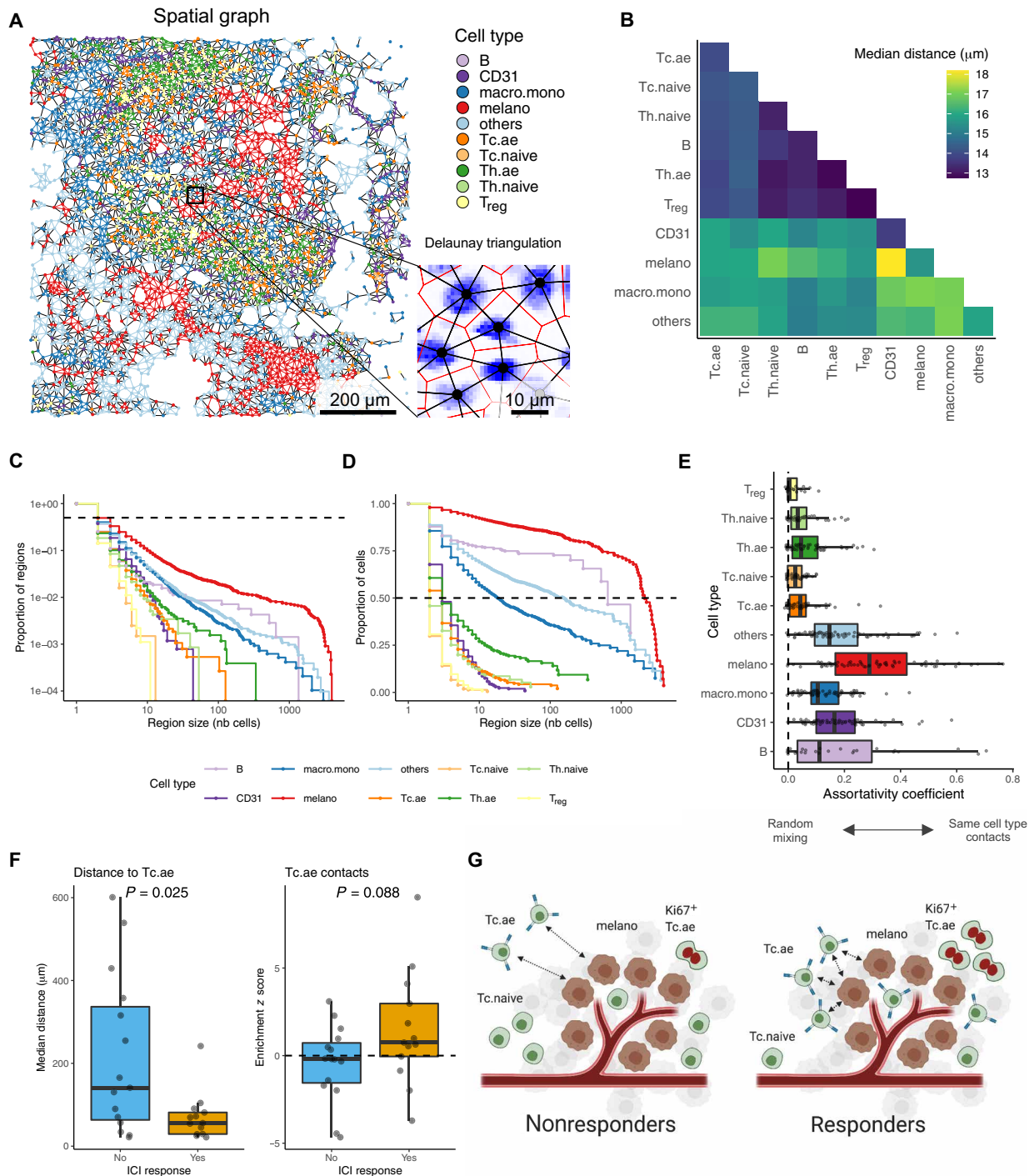
Fig. 5. Enrichment in contact between antigen-experienced T cells and melanomas favors ICI response. (**A**) Spatial graph obtained by Delaunay triangulation of cell locations in a melanoma sample. Each dot corresponds to the center of a cell identified by the nuclear segmentation pipeline and is colored according to cell type. Two cells were considered in contact if they were connected by a triangulation edge less than 30 μm in length. The smaller graph on the right illustrates how the triangulation (black edges) relates to a Voronoi diagram (red edges) likely corresponding to cell boundaries. For illustrative purposes, this graph is overlaid on top of intensity levels for the histone H3 marker. Each pixel corresponds to 1 μm². (**B**) Heatmap showing the median distance (in micrometers) observed between pairs of neighboring cells with respect to cell types across all samples ($N = 72$). (**C**) Complementary empirical cumulative distribution function of region sizes across all tumors, stratified by cell types and plotted with logarithmic axes. (**D**) Proportion of cells found within regions of size equal or larger than a given value (logarithmic x axis). (**E**) Distribution of assortativity coefficient, a measure of mixing between cell types, across all tumor and nevi samples ($N = 72$). Each point corresponds to the value for a given cell type in a single tumor sample. (**F**) Distribution of median distance from melanoma cells to nearest Tc.ae (left) and contact enrichments z scores (right) for the ICI-treated melanoma samples having at least one Tc.ae cell ($N = 28$). Uncorrected P values obtained from two-sided Wilcoxon rank sum test. (**G**) Schematic of CD8⁺CD45RO⁺Ki67⁺ T cell organization in the pretreatment melanoma microenvironment of ICI nonresponders and responders.

positive correlation between these proportions and assortativity coefficients, reflecting the fact that the most abundant cell types (melano, macro.mono, and others) were usually the ones that showed the highest levels of colocalization (fig. S9C). Similarly, we observed that cells forming the largest connected regions, which included melanoma, B cells, and nonclassified cells (others), usually had the highest assortativity coefficients, whereas T lymphocytes had more random mixing patterns (Fig. 5E). However, cells from the endothelial lineage (CD31^{+}) had a relatively high assortativity coefficient in several samples, despite the small size of their connected regions. This reflected the high degree of organization of intratumoral vasculature, which appeared as circular or ovaloid shapes in vessel cross sections (example images of tumors with a varying range of assortativity coefficient for the melanoma and endothelial cell types; fig. S9D). These observations underscore the necessity of considering multiple metrics to comprehensively characterize the spatial organization of a given cell type within the tumor.

To identify potential relationships between the organization of the tumor microenvironment and response to ICIs, we next considered the median distance from melanoma cells to their nearest neighbor of each cell type, in each pretreatment melanoma that received ICI therapy. We observed that antigen-experienced T cells were located significantly closer to melanoma cells in pretreatment tumors from ICI responders compared with nonresponders ($P = 0.025$) (Fig. 5F, left). In addition, melanoma cells from nonresponders that had proximal antigen-experienced T cells tended to have higher expression of phospho-ERK compared with responders (fig. S10, A to E). Because the distance relationship could have been confounded by the proportion of each cell type within the tumors, we used a permutation approach to estimate contact enrichment/depletion while taking these proportions into account ([14]). Specifically, we kept the location of melanoma cells fixed within the tumors while permuting the labels of the surrounding cells to estimate null distributions for the expected number of contacts. We observed that melanoma cells were generally enriched in contacts with cells from the macrophage/monocyte and unclassified groups (others) and depleted in contacts with endothelial (CD31^{+}) cells (fig. S11A). These features were not associated with ICI response (table S5); however, consistent with our median distance approach, melanoma cells from ICI responders trended toward a larger enrichment of contacts with antigen-experienced T cells compared with nonresponders ($P = 0.088$) (Fig. 5F, right). These relationships held if we restricted the analysis to samples with at least 250 melanoma cells (fig. S11B; median enrichment scores for each possible ordered pair of cell types are shown in fig. S11C).

By excluding the melanoma cells from the permutation, we controlled for the effect of the tumor structure on contact frequencies. If melanoma cells were included in the permutation, their contacts with all other cell types generally appeared as depleted (negative z scores), and this depletion was strongly correlated with the assortativity coefficient of the melanoma cells (fig. S11D). This reflected the contribution of the tumor structure in preventing interactions with the immune and other cell populations. In our ICI-treated cohort, we did not observe a significant association between treatment response and the assortativity coefficient of the melanoma cells, nor with the Tc.ae contact enrichment scores computed without controlling for the tumor structure (table S5). Together, these results suggested that the physical proximity and contact frequency between antigen-experienced cytotoxic T cells and melanoma cells were correlates of ICI response that do not merely reflect differences in cell type proportions and tumor structure (Fig. 5G).

DISCUSSION

Here, we characterized the immune landscape, tumor vascularity, and stromal and tumoral cell composition by performing multiplex, single-cell spatial profiling of melanomas using CyTOF IMC. We profiled cell types according to their expression of immune checkpoints, key melanoma signaling molecules, and proliferation markers. This approach provided granularity for the characterization of essential immune, stromal, and tumoral components in the melanoma immune microenvironment. By performing cross-sample comparisons, we observed considerable heterogeneity in the degree of immune infiltration and microenvironment architecture, yet a hierarchy stood out in the organization of the immune infiltrate. This hierarchy was preserved across melanoma subtypes and parallels the pattern described for triple-negative breast cancer ([14]), potentially reflecting a fundamental property of the tumor immune microenvironment. The macrophage/monocyte lineage predominated across samples and showed the highest contact enrichments with melanoma cells. Cytotoxic T cells were the second most abundant, followed by T helper cells, T_{regs}, and B cells. This observation may potentially reflect a temporal sequence in which tumors become infiltrated or indicate a higher level of spatial organization, such as the progressive assembly of tertiary lymphoid structures, themselves associated with a favorable prognosis in ICI-treated patients ([30], [31]). However, the analysis of 1-mm^2 cores did limit our ability to identify tertiary lymphoid structures.

To verify whether the TMA used for our CyTOF IMC analysis was generally representative of whole tissue slides, we performed a multiplex immunofluorescence microscopy experiment and compared cell proportions for multiple immune lineages. We found a significant positive correlation between full slides and TMA cores for CD4$^+$/T helper cells, CD8$^+$/cytotoxic T cells, and FoxP3/T_{regs} but did not see a significant correlation for CD20$^+$ cells. We believe that this is due, in part, to the higher variability of B cells within melanomas, which are generally present in low numbers but can be affected by the site of metastasis involving lymph nodes. Lymph node metastases, for instance, are particularly heterogeneous in their B cell population density. Furthermore, future studies will be needed to elucidate the spatial temporal changes that take place within the tumor immune microenvironment. Multiplexed single-cell imaging approaches that include CyTOF IMC ([14], [32–35]) are uniquely positioned to address this question by examining longitudinal biopsies throughout the trajectory of the disease and during treatment.

Our spatial analysis identified correlates of ICI response through proximity profiling and contact enrichment. Namely, a closer distance between melanoma cells and their nearest antigen-experienced cytotoxic T cells was associated with a favorable response. Once primed by an APC, cell killing by antigen-experienced T cells is largely dependent on perforin damage to the cell membrane and granzyme B damage to the nuclear envelope ([36]). Human and mouse model studies show that melanoma cells have the potential to recover from initial sublethal events and may require two or three interactions with an activated cytotoxic T cell within a short interval to become apoptotic ([37]). Prolonged presence and high abundance of antigen-experienced T cells within the melanoma microenvironment would allow for swarming and multiple contacts, leading to more effective

killing (*37*). This finding adds to a growing body of evidence supporting the importance of spatial relationships within the tumor microenvironment (*38*). For example, the expression of immune checkpoints by tumor cells and infiltrating lymphocytes as well as the proximity between ligand-receptor pairs (such as PD1–PD-L1 distance) correlate with clinical outcomes (*6, 39*). Ongoing physical contact between these receptors and their cognate antigens is likely involved in sustaining an immunosuppressive effect, and agents targeting PD1 work best when this interaction is observed in the pretreatment tumor microenvironment. Thus, assays that provide spatial information allowing quantification of cellular contacts will be crucial in the development of ICI biomarkers.

Pretreatment stratification of patients with advanced melanoma according to their likelihood of response to ICIs remains an elusive goal in precision oncology. Antigen-experienced cytotoxic T cells are a common target of both anti-CTLA4 and anti-PD1 agents (*12, 40*). Here, we found that patients with a higher proportion of proliferating, antigen-experienced cytotoxic T cells in pretreatment biopsies were more likely to respond to ICIs and had an improved overall survival. This subset of cytotoxic T cells has been characterized elsewhere as a dysfunctional compartment, expressing higher levels of PD1, TIM3, and LAG3 (*41*). As illustrated in murine models, intratumoral T cell phenotypes exist along a continuum of dysfunction (*42–44*). In the earlier stages of dysfunction, T cells are still amenable to rescue with checkpoint blockade, whereas in the later stages they become exhausted and resist reinvigoration with anti-PD1 therapies (*45–48*). The distinction between these two states and their impact on ICI response remains an area of active study in human melanomas.

The multiplex spatial proteomic profiling of the melanoma immune microenvironment described here allowed for a deep characterization at the single-cell level, not achievable by immunohistochemistry and conventional immunofluorescence assays. A recent melanoma study confirms a number of known correlates of ICI response using CyTOF IMC but uses binary masks to define cell type compartments within IMC images, highlighting some of the technical challenges that remain for cell segmentation and single-cell analysis (*49*). We recognize a number of remaining hurdles for the CyTOF IMC technology, which include intersample staining heterogeneity, relatively lengthy acquisition times, and complex analysis of image stacks. However, as workflows are optimized and technical advances allow for more detection channels, we envision its use to be expanded for three-dimensional profiling of tumor space and subcellular localization of protein signals to extract additional single-cell level information from patient-derived samples, as recently described (*50*).

In summary, we performed in-depth single-cell profiling of the melanoma immune microenvironment, preserving spatial information and tissue architecture. With this approach, we highlighted determinants of immunotherapy response and revealed fundamental features of the melanoma microenvironment. As the complex interactions within the tumor microenvironment are elucidated, it is increasingly clear that such profiling technologies could inform clinical decision-making and personalize therapeutic approaches.

MATERIALS AND METHODS
Study design
This study had two primary aims: (i) to characterize the melanoma immune microenvironment and (ii) to identify pretreatment correlates of response to ICIs. Aim (i) used both ICI-treated and

non–ICI-treated cohorts comprising 72 melanoma and nevi samples. Aim (ii) was addressed using 30 pretreatment samples originating from patients who subsequently received ICIs. Single CyTOF IMC images were obtained from each patient sample, and all included patients had information regarding treatment response and overall survival.

Sample procurement
The non–ICI-treated cohort consisted of 42 cores from a TMA of melanocytic neoplasms purchased from a commercial source, the Biomax online tissue bank, which included benign nevi, primary melanomas, and lymph node metastases (www.biomax.us/tissue-arrays/Melanoma/ME1004g). The second cohort of 30 pretreatment samples from ICI-treated patients with advanced melanoma was identified with the help of the McGill University Health Centre (MUHC) medical oncology department. The study was approved by our local Institutional Review Board in accordance with the precepts established by the Helsinki Declaration. Tissue samples were obtained from pretreatment archival pathology specimens as formalin-fixed paraffin-embedded (FFPE) tissue blocks. A representative hematoxylin and eosin slide was prepared for each sample and reviewed by a dedicated dermatopathologist at our institution. We identified representative areas of viable tumor for each specimen and mapped these areas of interest to the FFPE tissue blocks. We then constructed a TMA with 1-mm-sized cylindrical cores to allow simultaneous staining and acquisition of the whole patient cohort.

Antibody validation
Antibodies obtained directly from Fluidigm were validated by immunofluorescence on tonsil and melanoma tissues to confirm adequate staining intensity, optimal signal-to-noise ratio, and expected staining patterns with a clinical pathologist. For antibodies used in this study that were not available as conjugates to rare metal isotopes, we obtained a carrier-free aliquot of purified monoclonal antibody and performed immunofluorescence microscopy on a TMA containing a collection of melanoma, tonsil, lymph node, and breast and lung cancer tissues.

The potential for cross-talk was taken into account at the time of panel design and antibody titration. There is generally little cross-talk between channels on the IMC platform, usually not exceeding 5% (*51*), and predominantly affecting adjacent channels. We have therefore avoided placing lineage markers in the channels most affected by cross-talk and visually evaluated the signal spillover. Antibody titration was performed using twofold dilutions three times. Appropriate positive and negative tissue controls were selected and included spleen and melanoma samples. The working titer was selected for each antibody to maximize the signal-to-noise ratio across tissues while minimizing cross-talk across channels.

The Ventana DISCOVERY ULTRA autostainer was used for the deparaffination and antigen retrieval steps. Nonspecific binding sites were blocked with protein blocking solution (Dako, #X090930-2), and serial dilutions of the primary antibody were prepared in a total volume of 100-μl antibody diluent (Dako, #S080983-2). The TMA was completely covered with the antibody solution and was incubated overnight at 4°C in a humidity chamber. The following day, the tissue was washed 3 × 5 min in phosphate-buffered saline–Tween 20 (PBS-T) and stained with the secondary antibody (dilution 1:500) Alexa Fluor 488 donkey anti-rabbit (Invitrogen, #A32723) or Alexa Fluor 594 donkey anti-mouse (Invitrogen, #A32740) for 1 hour at

room temperature with gentle rocking. The slide was then washed 3 × 5 min in PBS-T and counterstained with 4′,6-diamidino-2-phenylindole (DAPI) (300 nM; Invitrogen, #D1306) for 10 min at room temperature. The slide was washed 3 × 5 min in PBS and then mounted using the Shandon Immu-Mount preparation (Thermo Fisher Scientific, #9990402).

After drying overnight, the slides were imaged using Zeiss Axio Scan Z1 and the immunofluorescence images were reviewed by a clinical pathologist. Antibody clones that did not perform well at this step were discarded (high background noise, nonspecific staining, and weak signal). The antibody clones with optimal signal-to-noise ratio were selected for each marker of interest and conjugated to a rare metal isotope using the Fluidigm Maxpar Antibody Labeling Kit according to the manufacturer's instructions. Once conjugated, the antibody was retested on the IMC platform to confirm continued performance, adequate signal-to-noise ratio, and expected staining pattern in immune and tumor tissues. Slightly different antibody panels were used on the two TMAs (tables S2 and S3).

Tissue processing

A 4-µm-thick section of the TMA was placed on a microscopy slide, which was processed in a workflow analogous to immunohisto-chemistry slide preparation. Briefly, the Ventana DISCOVERY ULTRA autostainer was used for the deparaffination and antigen retrieval steps. Nonspecific binding sites were blocked with the Dako protein block (catalog no. X090930-2), and the antibody cocktail was prepared in a total volume of 100-µl Dako antibody diluent (catalog no. S080983-2). The tissue was completely covered with the antibody cocktail and incubated overnight at 4°C in a humidity chamber. After three 5-min washing steps with PBS-T, the slide was stained with a nuclear intercalator solution containing iridium 193 and 191 isotopes for 20 min. The slide was then washed in ultrapure water and left to dry.

IMC data acquisition

IMC images were acquired with the Hyperion Imaging System (Fluidigm) coupled to a Helios mass cytometer (Fluidigm). All acquisitions were performed according to the manufacturer's instructions. Briefly, after daily calibration, the TMA tissue slide was subjected to laser ablation at a resolution of ~1 µm and a frequency of 200 Hz. About 1 × 1 mm region of interest from each TMA core was selected, and the TMA data were acquired in three batches. All IMC data were stored as MCD files and txt files. Individual MCD files were reviewed manually, confirming the presence of staining in each channel across all acquired samples. Poor-quality TMA cores containing few cells or with large necrotic areas were excluded from analysis. Samples with no melanoma cells (defined by the presence of SOX10 and/or S100 staining) were also excluded. Antibodies in our panels recognizing CCR7, CD47, CD56, and HLA-DR had clear nonspecific staining using conditions described above upon acquisition of IMC data using conditions described above and were omitted from downstream analysis.

Cell segmentation

Cells were segmented in a method adapted from (21), in which a pixel expansion around the segmented nuclei was used to identify cellular extension. Three channels were used to segment the nuclei: histone H3, Ir191, and Ir193. The quality of histone and iridium binding was validated visually before segmentation. Some samples

did not have good binding of iridium, and for these, we used histone solely to identify nuclei. Briefly, .mcd files were converted to stacked and individual channel .tiff files. Then, using CellProfiler (52), these stacked histone and iridium or histone-only images were processed to remove hot pixels, and areas from these images were randomly cropped and converted to .h5 files for compatibility with the ilastik software (23). In ilastik, image pixels were annotated as nuclear or nonnuclear, and the ilastik machine learning algorithm was trained on manual annotations to distinguish between nuclear and background regions. This step of supervised learning generated probability maps, which were exported for each sample and batch-applied to the complete images. These probability maps were then returned to CellProfiler to perform the nuclear segmentation. Nuclei were identified as primary objects with a diameter between 4 and 50 pixels (i.e., objects smaller than 4 µm in diameter or larger than 50 are discarded). Cell objects were defined from the nuclei by adding a 5-pixel circumferential expansion. The matrix of marker intensities was generated in CellProfiler by calculating the mean pixel intensity in each cell for each channel. When measuring the pixel intensity per cell, CellProfiler uses a hot pixel threshold to filter out antibody aggregates. Cellular segmentation allows for background staining not associated with a nucleus to be ignored in downstream analyses.

Cell type identification
Initial clustering

The lineage markers CD45, CD3, CD8, CD4, CD20, SOX10, S100, CD68, CD14, and CD31 were used for the initial classification step. Mean intensities were normalized per cell by logarithmizing (base10) and scaling for each channel, using the R's scale() function without centering. This step was performed independently for each cohort and helps address staining heterogeneity as well as varying levels of background signal. The matrix of scaled intensities was processed using the PhenoGraph clustering algorithm (22) using a value of 15 for the "nearest neighbors" parameter. Data obtained from separate TMA slides for the non–ICI-treated and ICI cohorts were clustered independently, and in both cases, PhenoGraph generated 47 clusters. From these 47 clusters, 8 were biologically relevant seed clusters for the ICI cohort and 10 for the non–ICI-treated cohort based on the distribution of channel intensities. Specifically, clusters were selected if they had maximal expression of their associated identity markers as well as low expression for all other identity markers: B (high CD20), CD4.T (high CD45, CD3, and CD4), CD8.T (high CD45, CD3, and CD8), CD31 (high CD31), macro.mono (high CD68 and/or CD14), melano (high SOX10 and/or S100), and other (low for all identity markers). The melano cluster is composed of two merged PhenoGraph clusters: one with high expression of SOX10 and low expression of all other identity markers and the other with moderate expression of both SOX10 and S100. Clusters corresponding to the same set of rules were merged to obtain a single cluster per cell type.

Cell reassignment of ICI-treated dataset

To improve classification, we reassigned cells using the k-means algorithm and mean intensities of the clusters identified above as initial cluster centers. Cells nearly equidistant to two or more clusters (distance ratio greater than 0.97) were considered to have ambiguous expression profiles and were reclassified with the others group.

Cell reassignment of ICI-untreated dataset

Because the k-means approach did not lead to a stable solution in the ICI-untreated dataset, cells were reassigned to the nearest cluster considering the Euclidean distance to the cluster centers. Cells that were at more than three distance units from all of the initial clusters were reclassified with the other group.

Immune cell subclassification

Cells in the CD4.T cluster were further subdivided into T_{regs} and T helper cells based on FoxP3 expression. CD4.T cells positive for FoxP3 were labeled T_{regs}, and those negative for FoxP3 were labeled Th. Next, cytotoxic T cells (CD8.T) and T helper cells were further subdivided into naive and antigen-experienced subsets. The former, lacking CD45RO expression, were labeled Tc.naive and Th.naive, whereas the latter, expressing CD45RO, were labeled Tc.ae and Th.ae, respectively. The CD45RO and FoxP3 subdivisions were performed using ilastik probabilities (see methods on ilastik object classification below).

ilastik object classification

For a number of markers (FoxP3, CD45RO, Ki67, and all checkpoints), we determined positivity at the cell level using the object classification module from ilastik (23). In this workflow, an object is defined as a set of pixels belonging to the same cell and a random forest is trained for classification. On the basis of the segmentation defined above and raw channel intensities, we manually annotated cells with clear intracellular signal as positive and cells without signal as negative. When ilastik predicted signal positivity as expected based on the raw signal, the prediction probabilities were exported for each image. Usually about 10 annotated cells per image were enough to generate accurate ilastik predictions. The exported results consist of one probability value per marker per cell. In downstream analyses, a cell was considered positive when its probability was greater than or equal to 0.5 and negative otherwise. This method helps filter out background signal by using manual annotation to determine true positive signal associated with segmented cells.

Cell presence-absence analysis

The presence or absence of a given cell type within each sample was determined using multiple thresholds: 30, 50, or 70 cells. If a sample contained the threshold number of cells of a given cell type or more, then the cell type is considered "present" in that sample, otherwise that cell type is considered "absent." The significance of co-occurrence of immune cell types was evaluated using Fisher's exact tests.

Comparison between responders and nonresponders

Patients were stratified into two groups according to the irRC (20). Patients were included in the responder group if they had a CR, a PR, or an SD. Patients with PD were considered nonresponders. We compared the proportion of each cell type between responders and nonresponders using a Wilcoxon rank sum test.

Survival analysis

For each cell type tested, patients of the ICI-treated cohort were stratified into two groups (high and low) using the median proportion for that cell type across samples as the partition point. Kaplan-Meier curves were plotted in R comparing these two groups. Time zero was defined as the time of treatment initiation, and P values were calculated using a log-rank test.

Spatial analysis

Because the distance between the nucleus of neighboring cells varies depending on their size and the degree of cellular agglomeration, we used Delaunay triangulation to identify pairs of cells that are most likely in physical contact (see Fig. 5A). We modeled the resulting cell network according to graph theory (53), with vertices representing cells and edges representing direct contacts between cells. Because the contact frequencies between different cell types are correlated with these cell type proportions, we used two parallel methods to obtain contact enrichment scores: a previously described cell shuffling algorithm (14, 54) as well as the assortativity index (29). Briefly, the shuffling method consists of performing 1000 permutations of the cell labels within the tumor microenvironment and recording contact frequencies. The overall procedure is used to generate a null distribution under the assumption of spatial independence between cell types. This null distribution is then compared with the number of contacts observed in our samples to compute a z score representing the degree of significance. Connected regions (components) within spatial graphs were identified using the "components" function of the "igraph" R package. The assortativity coefficient was calculated for each cell type in relation to all other types (considered as a single type) using the nominal assortativity formula (29). A value of 1 would indicate perfect assortative mixing, where contacts occur only between cells from the same type. A value of zero would indicate random mixing between cell types. A negative value would indicate disassortative mixing, a preference for contacts between cells from different types. All statistical analyses were performed with R version 4.1.0. Figure 5G was generated using Biorender.com.

Multiplex immunofluorescence imaging

The Akoya Biosciences Opal 7-color Manual IHC Kit (catalog number NEL811001KT) was used for the multiplex immunofluorescence imaging assay. Vendor specifications were followed during the staining protocol. Briefly, we performed dewaxing and rehydration, followed by antigen retrieval with the provided buffers (AR6 and AR9) using a pressure cooker for 5 min, followed by cooling at room temperature for 15 min. The provided antibody diluent was used for protein blocking.

The first validation experiment was performed on whole slide images from the same samples as the immunotherapy CyTOF cohort. In this assay, the antibody concentrations and fluorophore used were CD4 clone EP204 (1:100; Opal 520, AR9), CD8 clones C8/144B (1:300; Opal 570, AR9), CD68 clone KP1 (1:1000; Opal 650, AR9), CD20 clone L26 (1:100; Opal540, AR6), FoxP3 clone D608R (1:300; Opal 620, AR6), Sox10 clone 20B7 (Thermo Fisher Scientific) (1:100; Opal590, AR6), and PD-L1 clone E1L3N (CST) (1:100; Opal690, AR6). DAPI was used for nuclear staining, and Shandon Immu-Mount was used for mounting (Thermo Fisher Scientific, catalog number 28-600-42). Image acquisition was performed with a Zeiss 510 confocal microscope with online digital fingerprinting for our target channels. Downstream analysis for cell segmentation and phenotyping was performed using the Halo software (version 3.2.1851.354), with the module HighPlex FL 4.0.4.

The second validation experiment was performed on whole slide images from an independent, immunotherapy-treated cohort of 25 patients (8 with anti-PD1, 13 with anti-CTLA4, and 4 with both anti-PD1 and anti-CTLA4). In this assay, the antibody concentrations and fluorophores used were Ki67 clone B56 (1:50; Opal620, AR6), CD45RO clone UCHL-1 (1:200; Opal 690, AR6), Sox10 clone

SP267 (prediluted) (1:2; Opal520, AR6), and CD8a clone C8/144B (1:200; Opal570, AR9). DAPI was used for nuclear staining, and Shandon Immu-Mount was used for mounting (Thermo Fisher Scientific, catalog number 28-600-42).

Whole slides were scanned using the Zeiss Axio Scan Z1 system in immunofluorescence mode. Depending on the tumor area available on each slide, two to four regions measuring 4 mm^2 were extracted from each slide for further downstream analysis due to the computational requirements for the linear unmixing step. Linear unmixing was performed using the built-in module of the Zeiss Zen version 2.3 (Blue edition) software. For both immunofluorescence validation experiments, downstream analysis for cell segmentation and phenotyping was performed using the Halo software (version 3.2.1851.354), with the module HighPlex FL 4.0.4.

Statistics

We used nonparametric tests in this study. Two-sided Wilcoxon rank sum tests were used to perform two-sample tests in Figs. 4 (A and B) and 5F and figs. S6A, S7 (C and D), S10 (A to C), and S11B. Kruskal-Wallis rank sum tests were used to compare multiple distributions in fig. S5 (A, B, and D). Fisher's exact tests were used in Fig. 3C to detect associations. Spearman's rank correlation was used in figs. S8 (A and B), S9C, and S11D. Mantel-Haenszel log-rank tests were used to compare survival between two groups in Fig. 4C and figs. S7 (B and E) and S8C. All tests were done with R version 4.1.0, using an alpha level of 0.05 without adjustment for multiple testing.

SUPPLEMENTARY MATERIALS

www.science.org/doi/10.1126/sciimmunol.abi5072
Figs. S1 to 11
Tables S1 to S5

View/request a protocol for this paper from *Bio-protocol*.

REFERENCES AND NOTES

1. R. Alkallas, M. Lajoie, D. Moldoveanu, K. V. Hoang, P. Lefrançois, M. Lingrand, M. Ahanfeshar-Adams, K. Watters, A. Spatz, J. H. Zippin, H. S. Najafabadi, I. R. Watson, Multi-omic analysis reveals significantly mutated genes and DDX3X as a sex-specific tumor suppressor in cutaneous melanoma. *Nat. Cancer* 1, 635–652 (2020).
2. C. U. Blank, J. B. Haanen, A. Ribas, T. N. Schumacher, The "cancer immunogram". *Science* 352, 658–660 (2016).
3. Y. Ishida, Y. Agata, K. Shibahara, T. Honjo, Induced expression of PD-1, a novel member of the immunoglobulin gene superfamily, upon programmed cell death. *EMBO J.* 11, 3887–3895 (1992).
4. D. R. Leach, M. F. Krummel, J. P. Allison, Enhancement of antitumor immunity by CTLA-4 blockade. *Science* 271, 1734–1736 (1996).
5. J. J. Luke, K. T. Flaherty, A. Ribas, G. V. Long, Targeted agents and immunotherapies: Optimizing outcomes in melanoma. *Nat. Rev. Clin. Oncol.* 14, 463–482 (2017).
6. P. C. Tumeh, C. L. Harview, J. H. Yearley, E. J. Taylor, L. Robert, B. Chmielowski, M. Spasic, G. Henry, V. Ciobanu, A. N. West, M. Carmona, C. Kivork, E. Seja, G. Cherry, A. J. Gutierrez, T. R. Grogan, C. Mateus, G. Tomasic, J. A. Glaspy, R. O. Emerson, H. Robins, R. H. Pierce, D. A. Elashoff, C. Robert, A. Ribas, PD-1 blockade induces responses by inhibiting adaptive immune resistance. *Nature* 515, 568–571 (2014).
7. W. Hugo, J. M. Zaretsky, L. Sun, C. Song, B. H. Moreno, S. Hu-Lieskovan, B. Berent-Maoz, J. Pang, B. Chmielowski, G. Cherry, E. Seja, S. Lomeli, X. Kong, M. C. Kelley, J. A. Sosman, D. B. Johnson, A. Ribas, R. S. Lo, Genomic and transcriptomic features of response to anti-PD-1 therapy in metastatic melanoma. *Cell* 165, 35–44 (2016).
8. M. S.-Feldman, K. Yizhak, S. L. Bjorgaard, J. P. Ray, C. G. de Boer, R. W. Jenkins, D. J. Lieb, J. H. Chen, D. T. Frederick, M. Barzily-Rokni, S. S. Freeman, A. Reuben, P. J. Hoover, A. C. Villani, E. Ivanova, A. Portell, P. H. Lizotte, A. R. Aref, J. P. Eliane, M. R. Hammond, H. Vitzthum, S. M. Blackmon, B. Li, V. Gopalakrishnan, S. M. Reddy, Z. A. Cooper, C. P. Paweletz, D. A. Barbie, A. Stemmer-Rachamimov, K. T. Flaherty, J. A. Wargo, G. M. Boland, R. J. Sullivan, G. Getz, N. Hacohen, Defining T cell states associated with response to checkpoint immunotherapy in melanoma. *Cell* 175, 998–1013.e20 (2018).
9. C. Krieg, M. Nowicka, S. Guglietta, S. Schindler, F. J. Hartmann, L. M. Weber, R. Dummer, M. D. Robinson, M. P. Levesque, B. Becher, High-dimensional single-cell analysis predicts response to anti-PD-1 immunotherapy. *Nat. Med.* 24, 144–153 (2018).
10. P. B. Subrahmanyam, Z. Dong, D. Gusenleitner, A. Giobbie-Hurder, M. Severgnini, J. Zhou, M. Manos, L. M. Eastman, H. T. Maecker, F. S. Hodi, Distinct predictive biomarker candidates for response to anti-CTLA-4 and anti-PD-1 immunotherapy in melanoma patients. *J. Immunother. Cancer* 6, 18 (2018).
11. T. N. Gide, C. Quek, A. M. Menzies, A. T. Tasker, P. Shang, J. Holst, J. Madore, S. Y. Lim, R. Velickovic, M. Wongchenko, Y. Yan, S. Lo, M. S. Carlino, A. Guminski, R. P. M. Saw, A. Pang, H. M. McGuire, U. Palendira, J. F. Thompson, H. Rizos, I. P. D. Silva, M. Batten, R. A. Scolyer, G. V. Long, J. S. Wilmott, Distinct immune cell populations define response to anti-PD-1 monotherapy and anti-PD-1/anti-CTLA-4 combined therapy. *Cancer Cell* 35, 238–255.e6 (2019).
12. S. C. Wei, J. H. Levine, A. P. Cogdill, Y. Zhao, N. A. S. Anang, M. C. Andrews, P. Sharma, J. Wang, J. A. Wargo, D. Pe'er, J. P. Allison, Distinct cellular mechanisms underlie anti-CTLA-4 and anti-PD-1 checkpoint blockade. *Cell* 170, 1120, 1133.e17 (2017).
13. T. Gruosso, M. Gigoux, V. S. K. Manem, N. Bertos, D. Zuo, I. Perlitch, S. M. I. Saleh, H. Zhao, M. Souleimanova, R. M. Johnson, A. Monette, V. M. Ramos, M. T. Hallett, J. Stagg, R. Lapointe, A. Omeroglu, S. Meterissian, L. Buisseret, G. Van den Eynden, R. Salgado, M. C. Guiot, B. Haibe-Kains, M. Park, Spatially distinct tumor immune microenvironments stratify triple-negative breast cancers. *J. Clin. Invest.* 129, 1785–1800 (2019).
14. L. Keren, M. Bosse, D. Marquez, R. Angoshtari, S. Jain, S. Varma, S. R. Yang, A. Kurian, D. Van Valen, R. West, S. C. Bendall, M. Angelo, A structured tumor-immune microenvironment in triple negative breast cancer revealed by multiplexed ion beam imaging. *Cell* 174, 1373, 1387.e19 (2018).
15. B. Mlecnik, G. Bindea, A. Kirilovsky, H. K. Angell, A. C. Obenauf, M. Tosolini, S. E. Church, P. Maby, A. Vasaturo, M. Angelova, T. Fredriksen, S. Mauger, M. Waldner, A. Berger, M. R. Speicher, F. Pages, V. Valge-Archer, J. Galon, The tumor microenvironment and Immunoscore are critical determinants of dissemination to distant metastasis. *Sci. Transl. Med.* 8, 327ra326 (2016).
16. T. Tsujikawa, S. Kumar, R. N. Borkar, V. Azimi, G. Thibault, Y. H. Chang, A. Balter, R. Kawashima, G. Choe, D. Sauer, E. El Rassi, D. R. Clayburgh, M. F. Kulesz-Martin, E. R. Lutz, L. Zheng, E. M. Jaffee, P. Leyshock, A. A. Margolin, M. Mori, J. W. Gray, P. W. Flint, L. M. Coussens, Quantitative multiplex immunohistochemistry reveals myeloid-inflamed tumor-immune complexity associated with poor prognosis. *Cell Rep.* 19, 203–217 (2017).
17. F. Azimi, R. A. Scolyer, P. Rumcheva, M. Moncrieff, R. Murali, S. W. McCarthy, R. P. Saw, J. F. Thompson, Tumor-infiltrating lymphocyte grade is an independent predictor of sentinel lymph node status and survival in patients with cutaneous melanoma. *J. Clin. Oncol.* 30, 2678–2683 (2012).
18. Cancer Genome Atlas Network, Genomic classification of cutaneous melanoma. *Cell* 161, 1681–1696 (2015).
19. O. Hamid, H. Schmidt, A. Nissan, L. Ridolfi, S. Aamdal, J. Hansson, M. Guida, D. M. Hyams, H. Gomez, L. Bastholt, S. D. Chasalow, D. Berman, A prospective phase II trial exploring the association between tumor microenvironment biomarkers and clinical activity of ipilimumab in advanced melanoma. *J. Transl. Med.* 9, 204 (2011).
20. J. D. Wolchok, A. Hoos, S. O'Day, J. S. Weber, O. Hamid, C. Lebbe, M. Maio, M. Binder, O. Bohnsack, G. Nichol, R. Humphrey, F. S. Hodi, Guidelines for the evaluation of immune therapy activity in solid tumors: Immune-related response criteria. *Clin. Cancer Res.* 15, 7412–7420 (2009).
21. N. Damond, S. Engler, V. R. T. Zanotelli, D. Schapiro, C. H. Wasserfall, I. Kusmartseva, H. S. Nick, F. Thorel, P. L. Herrera, M. A. Atkinson, B. Bodenmiller, A map of human type 1 diabetes progression by imaging mass cytometry. *Cell Metab.* 29, 755–768.e5 (2019).
22. J. H. Levine, E. F. Simonds, S. C. Bendall, K. L. Davis, A. D. Amir, M. D. Tadmor, O. Litvin, H. G. Fienberg, A. Jager, E. R. Zunder, R. Finck, A. L. Gedman, I. Radtke, J. R. Downing, D. Pe'er, G. P. Nolan, Data-driven phenotypic dissection of aml reveals progenitor-like cells that correlate with prognosis. *Cell* 162, 184–197 (2015).
23. S. Berg, D. Kutra, T. Kroeger, C. N. Straehle, B. X. Kausler, C. Haubold, M. Schiegg, J. Ales, T. Beier, M. Rudy, K. Eren, J. I. Cervantes, B. Xu, F. Beuttenmueller, A. Wolny, C. Zhang, U. Koethe, F. A. Hamprecht, A. Kreshuk, ilastik: Interactive machine learning for (bio) image analysis. *Nat. Methods* 16, 1226–1232 (2019).
24. L. Lu, J. Barbi, F. Pan, The regulation of immune tolerance by FOXP3. *Nat. Rev. Immunol.* 17, 703–717 (2017).
25. A. Rheinlander, B. Schraven, U. Bommhardt, CD45 in human physiology and clinical medicine. *Immunol. Lett.* 196, 22–32 (2018).
26. E. Becht, L. McInnes, J. Healy, C. A. Dutertre, I. W. H. Kwok, L. G. Ng, F. Ginhoux, E. W. Newell, Dimensionality reduction for visualizing single-cell data using UMAP. *Nat. Biotechnol.* 37, 38–44 (2019).
27. C. H. Kugel III, S. M. Douglass, M. R. Webster, A. Kaur, Q. Liu, X. Yin, S. A. Weiss, F. Darvishian, R. N. Al-Rohil, A. Ndoye, R. Behera, G. M. Alicea, B. L. Ecker, M. Fane, M. J. Allegrezza, N. Svoronos, V. Kumar, D. Y. Wang, R. Somasundaram, S. Hu-Lieskovan, A. Ozgun, M. Herlyn, J. R. Conejo-Garcia, D. Gabrilovich, E. L. Stone, T. S. Nowicki,

J. Sosman, R. Rai, M. S. Carlino, G. V. Long, R. Marais, A. Ribas, Z. Eroglu, M. A. Davies, B. Schilling, D. Schadendorf, W. Xu, R. K. Amaravadi, A. M. Menzies, J. L. McQuade, D. B. Johnson, I. Osman, A. T. Weeraratna, Age correlates with response to anti-PD1, reflecting age-related differences in intratumoral effector and regulatory T-cell populations. *Clin. Cancer Res.* **24**, 5347–5356 (2018).

28. F. Conforti, L. Pala, V. Bagnardi, T. De Pas, M. Martinetti, G. Viale, R. D. Gelber, A. Goldhirsch, Cancer immunotherapy efficacy and patients' sex: A systematic review and meta-analysis. *Lancet Oncol.* **19**, 737–746 (2018).

29. M. E. Newman, Mixing patterns in networks. *Phys. Rev. E Stat. Nonlin. Soft Matter Phys.* **67**, 026126 (2003).

30. R. Cabrita, M. Lauss, A. Sanna, M. Donia, M. Skaarup Larsen, S. Mitra, I. Johansson, B. Phung, K. Harbst, J. Vallon-Christersson, A. van Schoiack, K. Lovgren, S. Warren, K. Jirstrom, K. Olsson, K. Pietras, C. Ingvar, K. Isaksson, D. Schadendorf, H. Schmidt, L. Bastholt, A. Carneiro, J. A. Wargo, I. M. Svane, G. Jonsson, Tertiary lymphoid structures improve immunotherapy and survival in melanoma. *Nature* **577**, 561–565 (2020).

31. B. A. Helmink, S. M. Reddy, J. Gao, S. Zhang, R. Basar, R. Thakur, K. Yizhak, M. Sade-Feldman, J. Blando, G. Han, V. Gopalakrishnan, Y. Xi, H. Zhao, R. N. Amaria, H. A. Tawbi, A. P. Cogdill, W. Liu, V. S. LeBleu, F. G. Kugeratski, S. Patel, M. A. Davies, P. Hwu, J. E. Lee, J. E. Gershenwald, A. Lucci, R. Arora, S. Woodman, E. Z. Keung, P. O. Gaudreau, A. Reuben, C. N. Spencer, E. M. Burton, L. E. Haydu, A. J. Lazar, R. Zapassodi, C. W. Hudgens, D. A. Ledesma, S. Ong, M. Bailey, S. Warren, D. Rao, O. Krijgsman, E. A. Rozeman, D. Peeper, C. U. Blank, T. N. Schumacher, L. H. Butterfield, M. A. Zelazowska, K. M. McBride, R. Kalluri, J. Allison, F. Petitprez, W. H. Fridman, C. Sautes-Fridman, N. Hacohen, K. Rezvani, P. Sharma, M. T. Tetzlaff, L. Wang, J. A. Wargo, B cells and tertiary lymphoid structures promote immunotherapy response. *Nature* **577**, 549–555 (2020).

32. M. Angelo, S. C. Bendall, R. Finck, M. B. Hale, C. Hitzman, A. D. Borowsky, R. M. Levenson, J. B. Lowe, S. D. Liu, S. Zhao, Y. Natkunam, G. P. Nolan, Multiplexed ion beam imaging of human breast tumors. *Nat. Med.* **20**, 436–442 (2014).

33. F. J. Hartmann, D. Mrdjen, E. McCaffrey, D. R. Glass, N. F. Greenwald, A. Bharadwaj, Z. Khair, S. G. S. Verberk, A. Baranski, R. Baskar, W. Graf, D. Van Valen, J. Van den Bossche, M. Angelo, S. C. Bendall, Single-cell metabolic profiling of human cytotoxic T cells. *Nat. Biotechnol.* **39**, 186–197 (2021).

34. H. W. Jackson, J. R. Fischer, V. R. T. Zanotelli, H. R. Ali, R. Mechera, S. D. Soysal, H. Moch, S. Muenst, Z. Varga, W. P. Weber, B. Bodenmiller, The single-cell pathology landscape of breast cancer. *Nature* **578**, 615–620 (2020).

35. C. M. Schurch, S. S. Bhate, G. L. Barlow, D. J. Phillips, L. Noti, I. Zlobec, P. Chu, S. Black, J. Demeter, D. R. McIlwain, S. Kinoshita, N. Samusik, Y. Goltsev, G. P. Nolan, Coordinated cellular neighborhoods orchestrate antitumoral immunity at the colorectal cancer invasive front. *Cell* **182**, 1341–1359.e19 (2020).

36. P. Golstein, G. M. Griffiths, An early history of T cell-mediated cytotoxicity. *Nat. Rev. Immunol.* **18**, 527–535 (2018).

37. B. Weigelin, A. T. den Boer, E. Wagena, K. Broen, H. Dolstra, R. J. de Boer, C. G. Figdor, J. Textor, P. Friedl, Cytotoxic T cells are able to efficiently eliminate cancer cells by additive cytotoxicity. *Nat. Commun.* **12**, 5217 (2021).

38. T. N. Gide, I. P. Silva, C. Quek, T. Ahmed, A. M. Menzies, M. S. Carlino, R. P. M. Saw, J. F. Thompson, M. Batten, G. V. Long, R. A. Scolyer, J. S. Wilmott, Close proximity of immune and tumor cells underlies response to anti-PD-1 based therapies in metastatic melanoma patients. *Onco. Targets Ther.* **9**, 1659093 (2020).

39. F. Dammeijer, M. van Gulijk, E. E. Mulder, M. Lukkes, L. Klaase, T. van den Bosch, M. van Nimwegen, S. P. Lau, K. Latupeirissa, S. Schetters, Y. van Kooyk, L. Boon, A. Moyaart, Y. M. Mueller, P. D. Katsikis, A. M. Eggermont, H. Vroman, R. Stadhouders, R. W. Hendriks, J. V. Thusen, D. J. Grunhagen, C. Verhoef, T. van Hall, J. G. Aerts, The PD-1/PD-L1-checkpoint restrains T cell immunity in tumor-draining lymph nodes. *Cancer Cell* **38**, 685–700.e8 (2020).

40. A. A. Tarhini, H. Edington, L. H. Butterfield, Y. Lin, Y. Shuai, H. Tawbi, C. Sander, Y. Yin, M. Holtzman, J. Johnson, U. N. Rao, J. M. Kirkwood, Immune monitoring of the circulation and the tumor microenvironment in patients with regionally advanced melanoma receiving neoadjuvant ipilimumab. *PLOS ONE* **9**, e87705 (2014).

41. H. Li, A. M. van der Leun, I. Yofe, Y. Lubling, D. Gelbard-Solodkin, A. C. J. van Akkooi, M. van den Braber, E. A. Rozeman, C. U. Blank, H. M. Horlings, E. David, Y. Baran, A. Bercovich, A. Lifshitz, T. N. Schumacher, A. Tanay, I. Amit, Dysfunctional CD8 T cells form a proliferative, dynamically regulated compartment within human melanoma. *Cell* **176**, 775–789.e18 (2019).

42. F. Alfei, K. Kanev, M. Hofmann, M. Wu, H. E. Ghoneim, P. Roelli, D. T. Utzschneider, M. von Hoesslin, J. G. Cullen, Y. Fan, V. Eisenberg, D. Wohlleber, K. Steiger, D. Merkler, M. Delorenzi, P. A. Knolle, C. J. Cohen, R. Thimme, B. Youngblood, D. Zehn, TOX reinforces the phenotype and longevity of exhausted T cells in chronic viral infection. *Nature* **571**, 265–269 (2019).

43. J. C. Beltra, S. Manne, M. S. Abdel-Hakeem, M. Kurachi, J. R. Giles, Z. Chen, V. Casella, S. F. Ngiow, O. Khan, Y. J. Huang, P. Yan, K. Nzingha, W. Xu, R. K. Amaravadi, X. Xu,

G. C. Karakousis, T. C. Mitchell, L. M. Schuchter, A. C. Huang, E. J. Wherry, Developmental relationships of four exhausted CD8(+) T cell subsets reveals underlying transcriptional and epigenetic landscape control mechanisms. *Immunity* **52**, 825–841.e28 (2020).

44. A. C. Scott, F. Dundar, P. Zumbo, S. S. Chandran, C. A. Klebanoff, M. Shakiba, P. Trivedi, L. Menocal, H. Appleby, S. Camara, D. Zamarin, T. Walther, A. Snyder, M. R. Femia, E. A. Comen, H. Y. Wen, M. D. Hellmann, N. Anandasabapathy, Y. Liu, N. K. Altorki, P. Lauer, O. Levy, M. S. Glickman, J. Kaye, D. Betel, M. Philip, A. Schietinger, TOX is a critical regulator of tumour-specific T cell differentiation. *Nature* **571**, 270–274 (2019).

45. M. Philip, L. Fairchild, L. Sun, E. L. Horste, S. Camara, M. Shakiba, A. C. Scott, A. Viale, P. Lauer, T. Merghoub, M. D. Hellmann, J. D. Wolchok, C. S. Leslie, A. Schietinger, Chromatin states define tumour-specific T cell dysfunction and reprogramming. *Nature* **545**, 452–456 (2017).

46. A. Schietinger, M. Philip, V. E. Krisnawan, E. Y. Chiu, J. J. Delrow, R. S. Basom, P. Lauer, D. G. Brockstedt, S. E. Knoblaugh, G. J. Hammerling, T. D. Schell, N. Garbi, P. D. Greenberg, Tumor-specific T cell dysfunction is a dynamic antigen-driven differentiation program initiated early during tumorigenesis. *Immunity* **45**, 389–401 (2016).

47. Z. Chen, Z. Ji, S. F. Ngiow, S. Manne, Z. Cai, A. C. Huang, J. Johnson, R. P. Staupe, B. Bengsch, C. Xu, S. Yu, M. Kurachi, R. S. Herati, L. A. Vella, A. E. Baxter, J. E. Wu, O. Khan, J. C. Beltra, J. R. Giles, E. Stelekati, L. M. McLane, C. W. Lau, X. Yang, S. L. Berger, G. Vahedi, H. Ji, E. J. Wherry, TCF-1-centered transcriptional network drives an effector versus exhausted CD8 T cell-fate decision. *Immunity* **51**, 840, 855.e5 (2019).

48. R. Zander, D. Schauder, G. Xin, C. Nguyen, X. Wu, A. Zajac, W. Cui, CD4(+) T cell help is required for the formation of a cytolytic CD8(+) T cell subset that protects against chronic infection and cancer. *Immunity* **51**, 1028–1042.e24 (2019).

49. S. Martinez-Morilla, F. Villarroel-Espindola, P. F. Wong, M. I. Toki, T. N. Aung, V. Pelekanou, B. Bourke-Martin, K. A. Schalper, H. M. Kluger, D. L. Rimm, Biomarker discovery in patients with immunotherapy-treated melanoma with imaging mass cytometry. *Clin. Cancer Res.* **27**, 1987–1996 (2021).

50. L. Kuett, R. Catena, A. Özcan, A. Pluss; Cancer Grand Challenges IMAXT Consortium, P. Schraml, H. Moch, N. de Souza, B. Bodenmiller, Three-dimensional imaging mass cytometry for highly multiplexed molecular and cellular mapping of tissues and the tumor microenvironment. *Nat. Cancer* **3**, 122–133 (2022).

51. S. Chevrier, H. L. Crowell, V. R. T. Zanotelli, S. Engler, M. D. Robinson, B. Bodenmiller, Compensation of signal spillover in suspension and imaging mass cytometry. *Cell Syst.* **6**, 612–620.e5 (2018).

52. C. McQuin, A. Goodman, V. Chernyshev, L. Kamentsky, B. A. Cimini, K. W. Karhohs, M. Doan, L. Ding, S. M. Rafelski, D. Thirstrup, W. Wiegraebe, S. Singh, T. Becker, J. C. Caicedo, A. E. Carpenter, CellProfiler 3.0: Next-generation image processing for biology. *PLOS Biol.* **16**, e2005970 (2018).

53. M. Barthélemy, Spatial networks. *Phys. Rep.* **499**, 1–101 (2011).

54. D. Schapiro, H. W. Jackson, S. Raghuraman, J. R. Fischer, V. R. T. Zanotelli, D. Schulz, C. Giesen, R. Catena, Z. Varga, B. Bodenmiller, histoCAT: Analysis of cell phenotypes and interactions in multiplex image cytometry data. *Nat. Methods* **14**, 873–876 (2017).

Science Immunology

Spatially mapping the immune landscape of melanoma using imaging mass cytometry

Dan MoldoveanuLeeAnn RamsayMathieu LajoieLuke Anderson-TrocmeMarine LingrandDiana BerryLucas J.M. PerusYuhong WeiCleber MoraesRached AlkallasShivshankari RajkumarDongmei ZuoMatthew DanknerEric Hongbo XuNicholas R. BertosHamed S. NajafabadiSimon GravelSantiago CostantinoMartin J. RicherAmanda W. LundSonia V. Del RinconAlan SpatzWilson H. Miller Jr.Rahima JamalRéjean LapointeAnne-Marie Mes-MassonSimon TurcotteKevin PetreccaSinziana DumitraAri-Nareg MeguerditchianKeith RichardsonFrancine TremblayBeatrice WangMay CherguiMarie-Christine GuiotKevin WattersJohn StaggDaniela F. QuailCatalin MihalcioiuSarkis MeterissianIan R. Watson

Spacing of immune cells matters

A better understanding of the tumor immune microenvironment can determine biomarkers of immunotherapy effectiveness. Moldoveanu *et al.* used cytometry time-of-flight (CyTOF) imaging mass cytometry (IMC) to characterize the immune microenvironment of melanoma patient samples. CyTOF IMC identified the spatial arrangement and proximity of immune cells to each other. The researchers observed that a closer proximity of antigen-experienced cytotoxic T cells to melanoma cells intratumorally correlated to a patient's responsiveness to immune checkpoint blockade. Thus, spatial characterization of the tumor immune microenvironment using CyTOF IMC allows for the identification of prognostic biomarkers for immunotherapy.

View the article online
https://www.science.org/doi/10.1126/sciimmunol.abi5072
Permissions
https://www.science.org/help/reprints-and-permissions

Use of this article is subject to the Terms of service